

Article

A Coupled Approach to Compute the Dislocation Density Development during Czochralski Growth and Its Application to the Growth of High-Purity Germanium (HPGe)

Wolfram Miller ^{1,*}, Andrejs Sabanskis ², Alexander Gybin ¹, Kevin-P. Gradwohl ¹, Arved Wintzer ¹,
Kaspars Dadzis ¹, Jānis Virbulis ² and Radhakrishnan Sumathi ^{1,*}

¹ Leibniz-Institut für Kristallzüchtung (IKZ), Max-Born-Str. 2, 12489 Berlin, Germany; alexander.gybin@ikz-berlin.de (A.G.); kevin-peter.gradwohl@ikz-berlin.de (K.-P.G.); arved.wintzer@ikz-berlin.de (A.W.); kaspars.dadzis@ikz-berlin.de (K.D.)

² Institute of Numerical Modelling, University of Latvia, Jelgavas Street 3, LV-1004 Riga, Latvia; janis.virbulis@lu.lv (J.V.)

* Correspondence: wolfram.miller@ikz-berlin.de (W.M.); radhakrishnan.sumathi@ikz-berlin.de (R.S.)

Abstract: The evolution of the dislocation density during Czochralski growth is computed by the combination of global thermal calculations and local computation of the stress and dislocation density in the crystal. The global simulation was performed using the open-source software Elmer (version 8.4) and the local simulation with the open-source software MACPLAS (version of 23.1.2023). Interpolation both in space and time was used to transfer the boundary conditions from the global simulations to the local model, which uses a different mesh discretization and a considerably smaller time step. We applied this approach to the Czochralski growth of a high-purity Ge crystal. The heater power change predicted by the global model as well as the final dislocation density distribution in the crystal simulated by the local model are correlated to the experimental results.

Keywords: global simulation; Czochralski; germanium; thermal stresses; dislocations



Citation: Miller, W.; Sabanskis, A.; Gybin, A.; Gradwohl, K.-P.; Wintzer, A.; Dadzis, K.; Virbulis, J.; Sumathi, R. A Coupled Approach to Compute the Dislocation Density Development during Czochralski Growth and Its Application to the Growth of High-Purity Germanium (HPGe). *Crystals* **2023**, *13*, 1440. <https://doi.org/10.3390/cryst13101440>

Academic Editor: Andrey Prokofiev

Received: 11 September 2023

Revised: 22 September 2023

Accepted: 22 September 2023

Published: 28 September 2023



Copyright: © 2023 by the authors. Licensee MDPI, Basel, Switzerland. This article is an open access article distributed under the terms and conditions of the Creative Commons Attribution (CC BY) license (<https://creativecommons.org/licenses/by/4.0/>).

1. Introduction

Growth of germanium (Ge) semiconductor single crystals is typically performed using the Czochralski (Cz) method. Among many applications of Ge crystals [1], we would like to highlight radiation detectors to make precise measurements of high-energy rays like gamma or X-rays [2]. A hydrogen atmosphere is needed to ensure the high purity during the growth process, but this has the drawback of forming hydrogen di-vacancies, which act as charge traps in the detector. Dislocations can reduce such defects and diminish the charge trapping effects of them. Dislocation densities in the range of 10^3 cm^{-2} – 10^4 cm^{-2} lead to a good performance [3]. Consequently, engineering of the dislocations is required to obtain a nearly homogeneous distribution over the crystal in the required range. It is well known that the multiplication of dislocations is influenced by the stresses in a growing crystal. For example, low thermal stresses and dislocation densities can be achieved by specially designing the hot zone to reduce the temperature gradients [4].

Such dislocation engineering would be very helpful in conjunction with the Legend project [5], with the aim of detecting the neutrinoless double- β decay. High-purity germanium (HPGe) crystals are enriched in the isotope ^{76}Ge , which is predicted to undergo a neutrinoless double- β decay. Thus, the HPGe detector acts both as source and detector. Such experiments have been performed, e.g., in the GERDA project [6]. Further investigations will be performed within the Legend project [5], applying 200 kg of Ge detectors in the first step and 1000 kg in the second.

Numerical simulations are a valuable tool for detailed investigations of the Cz crystal growth, including such aspects as the global heat transfer, melt flow, thermal stresses, and

dislocation density distribution. While a large amount of literature exists on modelling the Cz Ge crystal growth, see, e.g., [7–9], computing the dislocation density evolution is still a great challenge. The time evolution of the temperature field in the growing crystal has to be calculated accurately considering the growth process in the furnace. On the other hand, the dislocation density dynamics has to be modelled in a growing crystal, which in most cases has been achieved by applying the Alexander–Haasen (AH) model [10]. This describes stress relaxation through plastic deformations and the multiplication of the dislocations depending on the local temperature and the effective stress. The Alexander–Haasen model does not take into account the propagation of dislocations. Thus, it is a simplification of reality, in which different kinds of dislocations can occur, such as screw and edge dislocations. In Czochralski-grown Ge crystals, screw dislocations are dominant [11]. In the classical Alexander–Haasen model, there is also no preferential direction, like gliding planes, defined where the line defects move. A deeper insight into the dislocation dynamics could be gained by discrete dislocation dynamics, with high computational costs for small spatial domains (see, e.g., [12]). Despite all of these restrictions, the Alexander–Haasen model has been used for various materials, such as GaAs and InP [13], multi-crystalline Si [14], and SiC [15].

One of the first realistic simulations of dislocation evolution during Cz growth of semiconductor crystals was carried out by Miyazaki and Okuyama [16]. They employed the AH model and considered Si, InP, and GaAs crystals with a diameter of 8". The temperature field was calculated at several discrete crystal lengths, and interpolated on a different mesh for the dislocation density simulations. The model was later extended to take into account the crystal anisotropy [17], finding that the dislocation density for the $\langle 111 \rangle$ growth direction is lower than for the $\langle 001 \rangle$ direction.

A similar approach of performing separate steady-state global heat transfer simulations which are then interpolated onto the mesh for dislocation density simulations has also been used by other researchers, see, e.g., [18,19]. However, recalculation of the temperature equation in the local crystal model with a finer mesh and a much lower time step was not performed. This could potentially lead to a reduced spatial resolution of the temperature field affecting the stress distribution, and to neglected transient effects.

A fully transient calculation was performed by Artemyev et al. for the Czochralski growth of Ge [8]. They used the software package CGSim to perform a transient calculation of the crystal growth in the cylindrical part of the process. Thus, the grids in melt and crystal were deformed during the computation. However, for the computation of the dislocation density the grid was different and not changing in time [20]. This requires adding nodes at the propagating crystal/melt interface and, subsequently, setting dislocation densities in the new nodes. They used two approaches for the setting, as described in more detail in [8]. They found a reasonable agreement with the six experimental data points of etch pit density (EPD). Because they considered a Czochralski growth with very low thermal gradients, provided by a very effective thermal insulation, there was no increase in the dislocation density from the middle of the crystal to the end.

For the growth of high-purity germanium sources, where impurities have to be minimised, such insulation is not possible. Consequently, the thermal gradients are much larger; also due to the high thermal conductivity of hydrogen (H_2), which is used as the gas environment. Wang et al. [21] obtained the axial temperature difference by measuring the temperature at two points using thermocouples yielding to thermal gradients of about 25 K cm^{-1} in the beginning up to 80 K cm^{-1} at the end of the growth process. They used the axial temperature gradient to estimate the dislocation density in the crystal in the sense of a very simple approximation.

In this paper, we present a coupled approach to computing the evolution of the dislocation density and apply it to the growth of an HPGe crystal. Details of the experimental setup and process are described in [22,23]. The coupled approach consists of an axisymmetric global simulation of the temperature field (with a larger time step) and a local calculation of the temperature, stress, and dislocation density only in the crystal (with a smaller time

step). The coupling is considered in one direction, i.e., the temperature at the surface of the crystal is transferred from the output of the global simulation to the boundary conditions in the local simulation. For the global simulation, we use the open-source software Elmer, and for the local one the open-source software MACPLAS [24], which has been already applied to a parametric study of dislocations in Ge crystals [25]. The coupled approach presented here is general and can be used for any Czochralski process.

2. Numerical Model

2.1. Global Calculation Using Elmer

Global axisymmetric simulations of the growth process were performed with the open-source software Elmer (version 8.4) [26], which is a finite element program with various solvers, such as for inductive heating, heat transfer, wall-to-wall radiation, melt convection, and phase change. For the mesh creation we applied gmsh (version 4.11.1) [27] through its Python API using an object-oriented approach based on “objectgmsh” [28], which simplifies meshing of complex geometries. Recently, a Python interface for Elmer, named “pyelmer”, has been developed [29]. Based on this interface, a framework for Czochralski growth called “openCGS” [30,31] has been established. The “openCGS” framework was extended to perform quasi-transient calculations as developed earlier [9]. In the current version, geometries for Czochralski growth are described in a more systematic way (see Figure 1): (1) crystal and crystal holder (type I, movable by crystal pull velocity); (2) crucible and crucible holder (type II, movable); (3) other parts (type III, fixed). In the Czochralski growth experiments for HPGe, the crucible position is fixed, i.e., objects of type II do not move. Thus, we only need to compute the position of the crystal and its holder.

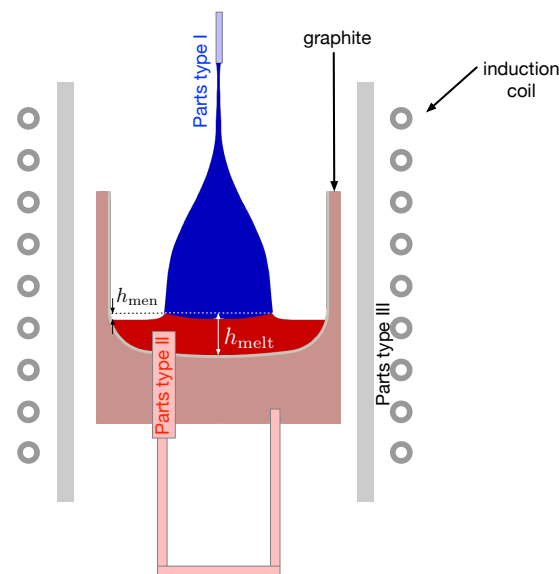


Figure 1. Simplified sketch of the experimental setup (further details cannot be shown due to confidentiality reasons). The different types of the parts are indicated. Parts of type I are in bluish colour (movable upwards), i.e., crystal and holder. Parts of type II are in reddish colour (movable downwards), i.e., melt (red), crucible and crucible holder. Parts of type III are in grey colour, i.e., insulation and induction coil. The definitions of the melt height h_{melt} and meniscus height h_{men} are also shown.

For geometry definition, openCGS has been extended with a set of functions that draw the complex furnace geometry based on the characteristic points of each body. A parameterisation allows the movable plant parts to be moved according to the current crystal length. The contact areas between the bodies are determined automatically and do not require further adjustment, e.g., when the melt height drops from the cylindrical to the bottom part of the crucible. For quasi-transient simulations, a new class was implemented in

openCGS, which automatically starts the individual steady-state simulations and performs basic evaluations. This general openCGS code is available open source.

The crystal shape is given as a set of data points (R, L) , which might originate from a grown crystal or define a target crystal shape. The first step is to compute the corresponding crystal mass. Because the crucible is completely emptied at the end of the growth process, the mass of the crystal corresponds to the mass of the melt at the beginning of the growth process. In the model, the surface of the crystal is represented by a spline function, which means we have a continuous function which is used to compute the growth angle for every time step. From the growth angle and the contact angle (14° for Ge) together with the crystal radius, the meniscus height h_{men} is computed using the approach of Hurlé [32]. Further details can be found in [9]. The melt volume is computed considering the meniscus but under the assumption of a flat crystal/melt interface. The interface shape is computed in the run and cannot be considered at this step. The (numerical) melt height h_{melt} is defined as shown in Figure 1.

The time loop is realised by increasing the length of the crystal by Δl in every time step. The growth velocity v_{growth} results from the pulling velocity v_{pull} and the decreasing melt height. v_{growth} is larger than the pulling velocity v_{pull} , since the melt level is always decreasing. v_{growth} enters the computation of latent heat release in the next time step. For the calculations presented in this paper, we used $\Delta l = 2$ mm and $\Delta l = 1$ mm to check the influence of the time step in the quasi-transient calculation.

Having the geometry of melt and crystal for the global calculation, the induced heat is computed. In the thermal field calculation, the induced heat is multiplied by a factor to meet the melting point temperature at the three-phase point. The thermal field calculation comprises wall-to-wall radiation, heat conduction, and convective heat transfer in the melt and gas. The convection in the melt and the gas is obtained by directly solving the Navier–Stokes equation. To achieve a converged solution, the viscosity was artificially increased.

In the melt we consider buoyancy convection, forced convection by the crystal, and crucible rotation, as well as Marangoni convection at the free surface. For the gas convection we consider buoyancy convection and set the velocity at all boundaries to zero, except at the inlet and the outlet. For comparison with MACPLAS we also compute the elastic stress in the crystal.

In every time step, we write out the temperature along the surface of the crystal. These data are used as the boundary condition in the local calculation with MACPLAS. The correctness of this procedure was checked by comparison of the stress field obtained with Elmer and a steady-state computation with MACPLAS.

2.2. Local Calculation Using MACPLAS

Since the results of the global calculation are only available at discrete crystal lengths, a local transient model has been developed to predict the time-dependent temperature and dislocation density distributions in the crystal. The local model uses the previously developed open-source solver package MACPLAS [24] which is based on the open-source finite element library deal.II [33]. MACPLAS has recently been applied to analyse thermally induced dislocation generation in floating-zone Si crystals [34] and dislocation dynamics in a parametric model for Czochralski Ge growth [25]. For the present study, the MACPLAS crystal growth solver has been extended with an option to import external temperature boundary conditions $T(r, z, t)$.

The time-dependent temperature field in the crystal is described by the equation

$$\rho c_p \frac{\partial T}{\partial t} = \nabla \cdot (\lambda \nabla T), \quad (1)$$

where ρ is the density, c_p —specific heat capacity, and λ —thermal conductivity. Heat transfer by convection is not included in the temperature equation, but is considered by the temperature update in each time step according to the shifts in the mesh nodes [25]. We chose to solve the local temperature Equation (1) instead of simply interpolating the whole

field from the global results, in order to obtain a more accurate T distribution on a finer local mesh and take into account the transient effects (at least partially, since temperature at the crystal surface is still taken from the steady-state global results).

A zero-flux boundary condition is set on the crystal axis; Dirichlet (first-type) boundary conditions are applied at the melt/crystal interface (melting point) and crystal side surface (non-homogeneous temperature profile from the global simulation). A steady-state temperature distribution is calculated and used as the initial condition at the beginning of the simulation at $t = 0$.

The crystal geometry and temperature field on the crystal surface (for Dirichlet boundary conditions) from global Elmer simulations are used in the local model. Since Elmer results are only available at certain crystal lengths, linear interpolation in time between the two closest crystal positions is employed to obtain the necessary data for the local simulation, similar to previous studies, cf. [16,18]. To correctly treat the time-varying crystal shape, the radial and axial coordinates are normalised by the crystal radius and crystal length, correspondingly.

For simplicity, the stretching mesh approach is used in the local model, i.e., without changing the number of points and without mesh regeneration. Additional aspects related to the mesh movement, such as the update of the temperature field to model the heat transfer by convection, are described in [25].

The macroscopic dislocation density dynamics is described by the Alexander–Haasen model [10]. The time evolution of the dislocation density N_m depends on the dislocation velocity v and the effective stress τ_{eff} :

$$\frac{dN_m}{dt} = Kv\tau_{\text{eff}}^l N_m, \quad (2)$$

where K and l are material constants. The dislocation velocity v is given by

$$v = k_0 \tau_{\text{eff}}^m \exp\left(-\frac{Q}{k_B T}\right) \quad (3)$$

with material constants k_0 and m , activation energy (Peierls potential) Q , and the Boltzmann constant k_B . The effective stress τ_{eff} is computed from the stress τ and strain hardening τ^* caused by a dense structure of dislocations:

$$\begin{aligned} \tau_{\text{eff}} &= \tau - \tau^* & \text{if } \tau > \tau^* \\ \tau_{\text{eff}} &= 0 & \text{if } \tau \leq \tau^*. \end{aligned} \quad (4)$$

τ^* is given by $\tau^* = D\sqrt{N_m}$ with the strain-hardening factor D . τ^* is only relevant for large dislocation densities. τ is defined by the second invariant of the stress deviator

$$\tau = \sqrt{J_2}, \quad \text{with } J_2 = \frac{1}{2} \sum_{i,j} S_{ij}^2. \quad (5)$$

$\sqrt{3J_2}$ is the von Mises stress. The stress deviator is defined via: $S_{ij} = \sigma_{ij} - \delta_{ij} \frac{1}{3} \sum_k \sigma_{kk}$. Here, δ_{ij} is the Kronecker symbol and σ_{ij} is the stress tensor.

In addition to the dislocation multiplication law (2), the Orowan relation in isotropic formulation is used in the AH model to describe the plastic strain components ε_{ij}^c :

$$\frac{d\varepsilon_{ij}^c}{dt} = \frac{bvN_m}{2\sqrt{J_2}} S_{ij}, \quad (6)$$

where b is the magnitude of the Burgers vector. Non-zero homogeneous dislocation density distribution and zero plastic strain are set at $t = 0$. For additional details regarding the AH model, we refer the reader to our prior works [25,34].

3. Material Parameters

3.1. Germanium

The physical properties for the melt are given in Table 1. We used a direct simulation of the melt flow and applied the steady-state Navier–Stokes equation without a turbulent model. For this reason we used an increased viscosity ($\mu = 3 \times 10^{-2}$ Pa s), which ensures a convergence of the steady-state Navier–Stokes solution. The melting point is $T_m = 1210$ K.

Table 1. Physical parameters of the Ge melt.

Density	ρ_m	kg m^{-3}	5534	*
Heat capacity	c_p	$\text{J kg}^{-1} \text{K}^{-1}$	358 (@ T_m)	[35]
Thermal expansion	α_V	K^{-1}	1.06×10^{-4}	[36]
Thermal conductivity	λ	$\text{W m}^{-1} \text{K}^{-1}$	48 (@ T_m)	[37]
Emissivity	ϵ		0.2	[38]
Electrical conductivity	σ_{el}	S m^{-1}	1.4×10^6	[39]
Dynamic viscosity	μ	Pa s	6.8×10^{-4} (@ T_m)	[40]
Prandtl number	Pr		0.05	
Marangoni coefficient		$\text{N m}^{-1} \text{K}^{-1}$	7.32×10^{-5}	[41]
Latent heat	ΔH	J kg^{-1}	4.65×10^5	[42]
Laplace constant	a_L	m	5.3×10^{-3}	

* Intermediate value between measurements of [35,40].

For the crystal, we used temperature dependent parameters if possible, because in the upper part of the crystal the temperature becomes lower than 700 K at later growth stages. All parameters for the Ge crystal are given in Table 2. More details on the origin of the functions given in the table are presented in Appendix A.

Table 2. Physical parameters of the Ge crystal.

Density	ρ_m	kg m^{-3}	5370 (@ $T = 300$ K)	†
Heat capacity	c_p	$\text{J kg}^{-1} \text{K}^{-1}$	418 (@ T_m)	[42]
Thermal expansion	α_L	K^{-1}	$(7.6 - 4.0 e^{-T/365 \text{ K}}) \times 10^{-6}$	*
Thermal conductivity	λ	$\text{W m}^{-1} \text{K}^{-1}$		
		$T \leq 300$ K	$4.669 \times 10^4 (1 \text{ K}^{-1} T)^{-1.16}$	*
		$30 \text{ K} < T \leq 1000$ K	$2.614 \times 10^4 (1 \text{ K}^{-1} T)^{-0.729}$	*
		$1000 \text{ K} < T$	17	*
Emissivity	ϵ		0.55	[43]
Electrical conductivity	σ_{el}	S m^{-1}	$e^{15.255 - 4317.3 \text{ K}/T}$	[44]
Elastic constants	C_{11}	Pa	$(13.2 \times 10^{10} - 1.7 \times 10^7 \text{ K}^{-1} T)$	*
	C_{12}	Pa	$(4.3 \times 10^{10} - 4.2 \times 10^6 \text{ K}^{-1} T)$	*
	C_{44}	Pa	$(7.1 \times 10^{10} - 1.07 \times 10^7 \text{ K}^{-1} T)$	*
Peierls energy	Q	eV	1.62	[45,46]
Prefactor in Equation (2)	K	m N^{-1}	4.0×10^{-3}	[12]
Prefactor in Equation (3)	k_0	$\text{m s}^{-1} \text{Pa}^{-1}$	6.9×10^{-3}	[12]
Exponent in Equation (2)	l		1	[12]
Exponent in Equation (3)	m		1	[12]

* See Appendix A. † for historical reasons we used a slightly larger value than given by [47]: 5330 kg m^{-3} . For transient computations, only $\rho_m c_p$ is relevant. For steady-state calculations the density does not matter at all.

The parameters for the Alexander–Haasen model (last section in Table 2) are derived from the discrete dislocation dynamics simulations by Gradwohl et al. [12], except the Peierls energy, which was taken from experiments [45,46].

3.2. Other Materials

The physical parameters for steel and quartz were taken as given in [9]. The quartz was treated as completely transparent for the thermal radiation. The data for the graphite susceptor are given in Table 3.

Table 3. Physical parameters used for graphite.

Density	ρ	kg m^{-3}	1750	
Heat capacity	c_p	$\text{J kg}^{-1} \text{K}^{-1}$	527	
Emissivity	ϵ		0.8	
Thermal conductivity	λ	$\text{W m}^{-1} \text{K}^{-1}$	$90 (1.29 - 1.09 \times 10^{-3} \text{K}^{-1} T + 4.016 \times 10^{-7} \text{K}^{-2} T^2 - 4.77 \times 10^{-11} \text{K}^{-3} T^3)$	[48]
Elec. conductivity	σ_{el}	S m^{-1}	$10^6 / (8.4 + (T - 1173 \text{K})^2 / 1.9 \times 10^5 \text{K}^2)$	[48]
			$10^6 / (8.95 + 0.65 \tanh((T - 1673 \text{K} / 350 \text{K})))$	[48]

For growing HPGe crystals, hydrogen is used as the gas atmosphere (typical pressure is $P = 0.1 \text{ MPa}$). The parameters were set as shown in Table 4.

Table 4. Physical parameters of H_2 gas.

Density	ρ	kg m^{-3}	$0.0617 (@P = 0.1 \text{ MPa}, T = 400 \text{ K})$	
Heat capacity	c_p	$\text{J kg}^{-1} \text{K}^{-1}$	$14,500 (@P = 0.1 \text{ MPa}, T = 400 \text{ K})$	
Heat conductivity	λ	$\text{W m}^{-1} \text{K}^{-1}$	$0.08 + 3.9 \times 10^{-4} \text{K}^{-1} T$	[49]
			$(@P = 0.25 - 0.4 \text{ MPa})$	
Thermal expansion	α_L	K^{-1}	$\frac{1}{3} T^{-1}$	ideal gas
Dynamic viscosity	μ	Pa s	1×10^{-3}	[50]
			$(@P = 0.1 \text{ MPa}, T = 350 \text{ K})$	

4. Experimental Setup

HPGe crystals are grown in equipment with inductive heating. The crucible holder is made of graphite and acts as a susceptor. All other parts in the inner region of the furnace consist of high-purity fused silica (referred to as quartz). A general description is given elsewhere [22] and a sketch is provided in Figure 1. The equipment is used to grow $3''$ crystals in the [001] direction using a quartz crucible for the melt. Crystals are pulled with a constant pulling velocity of $v_{\text{pull}} = 0.5 \text{ mm min}^{-1}$, except when the end cone is grown to empty the crucible. The position of the crucible is fixed during the entire process of crystal growth. This means that due to the decreasing melt level, the growth velocity becomes larger than the pulling velocity. The diameter of the crystal is controlled manually by adapting the heating power. In this paper, we consider an experiment with an ingot mass of 3091 g. During the growth experiment, the rotation rates of the crystal and crucible were 17 rpm and -3 rpm, respectively (counter rotation). The final crystal is shown in Figure 2. We use the shape of this crystal for our calculations. The shape was extracted from the projection on millimetre graph paper, as indicated by the black line at the upper part of the crystal in Figure 2. The two measured diameters (white lines in Figure 2) acted as a reference.

The dislocation density along the length of the crystal was investigated by EPD analysis according to the IEEE Standard Test Procedures for High-Purity Germanium Crystals for Radiation Detectors [51]. For this purpose, three oriented (001) wafers were cut from the crystal, as indicated by the thick orange lines in Figure 2. The wafers were chemo-mechanically polished and etched. A (001) HPGe dislocation etch was prepared, consisting of a parent solution of 25 g $\text{Cu}(\text{NO}_3)_2 \cdot 3\text{H}_2\text{O}$ in 500 mL deionized water (17 M Ω cm), 250 mL HNO_3 (70% per weight), and 500 mL HF (49% per weight). The wafers were immersed in the etch for 90 s, so that distinct dislocation etch pits were formed. The etch pits were counted and analysed using optical microscopy and differential interference contrast.

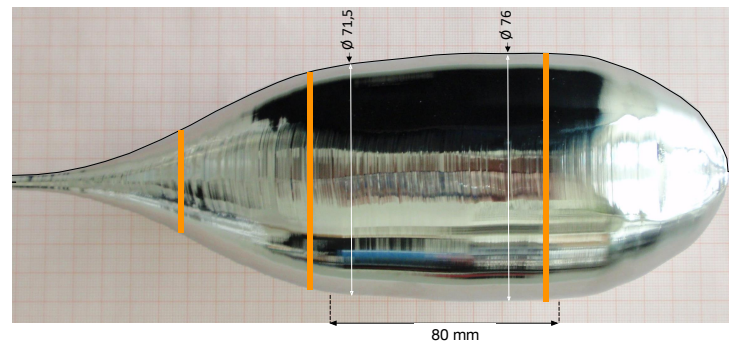


Figure 2. Experimentally grown crystal with the as-grown shape. The crystal is axisymmetric except in the end cone, where facets appeared. For numerical calculations, the shape is approximated by a spline function (see black line at top). The mass of the ingot in the experiment was 3091 g; the weight corresponding to the volume of the crystal for the simulation was slightly smaller, 2995 g. The thick orange lines indicate the cuts for the three wafers to be used in the EPD analysis.

5. Results and Discussion

5.1. Global Simulation (Elmer)

For HPGe, no lateral photovoltage scanning (LPS) measurements [52] are possible and, therefore, the interface deflection during growth is unknown. One way to compare the simulation with the experiment is the change in required power over time. In the computation, the power is measured as the power of the electrical current in the coils. The power is adapted to ensure the melting point temperature at the three-phase point. Please note that in the axisymmetric calculation, the coil is represented by rings—the number of rings corresponds to the number of windings in the real coil. In addition, all additional parts, such as current supplies, are not considered in the simulation. Furthermore, power losses in the generator are not considered in the model. Therefore, the absolute power is different in the experiment and simulation. Assuming that this difference is constant in the range of power change during the growth process, we can compare this change. Recently, investigations in model experiments on this problem have given a more detailed picture on power losses in induction heating systems [53], but there is not yet a general rule to be applied to our experiment.

In Figure 3, the change in power ΔP is shown for three numerical runs and the experiment. The reference for $\Delta P = 0$ is the minimal power in the experiment (at a time of 346 min) and in the simulations (at a time of 368 min). The black curve (computation without gas convection) is only slightly different from the two others. Thus, gas convection has only a weak influence on the power consumption. Hydrogen, as the high-purity gas, has quite a high thermal conductivity and, therefore, there is already a significant thermal transport by diffusion. When argon is used, gas convection plays a much stronger role. We also checked a different time stepping, i.e., using $\Delta l = 2$ mm in one case (red curve) and $\Delta l = 1$ mm in the other (orange curve). Nearly no difference can be seen in Figure 3.

In Figure 4 (left), the drop in the melt height h_{melt} is shown, which causes a higher growth rate than the pulling velocity since the crucible position is fixed. On the right-hand side, the increase in the growth velocity v_{growth} with increasing crystal length can be seen. There are only small differences in h_{melt} and v_{growth} between the runs with $\Delta l = 2$ mm and $\Delta l = 1$ mm.

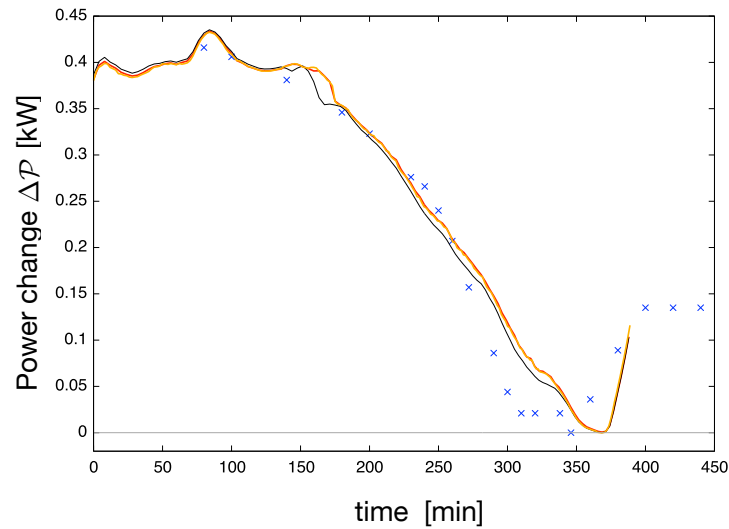


Figure 3. Power change as a function of growth time. \times : experimental values. Black curve: Computation without gas convection. Red and orange curves: Computations with gas convection. Calculations were performed with $\Delta l = 2$ mm (black and red) as well as with $\Delta l = 1$ mm (orange). The lowest power in the experiment defines the reference for the power change. Results of simulations are shifted to match the two points on the left-hand side.

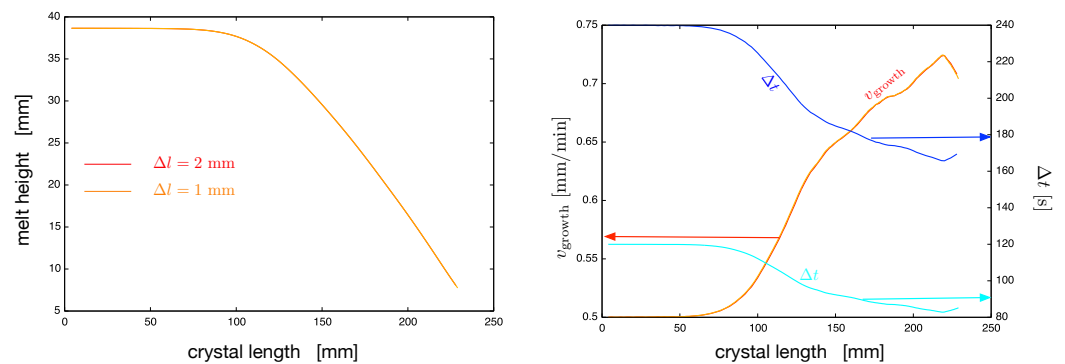


Figure 4. Melt height h_{melt} (left) and growth velocity (right) as a function of the growth stage in terms of crystal length. Red and orange curves are for $\Delta l = 2$ mm and 1 mm, respectively. In the right figure, also the time step Δt for the computation is shown (blue for $\Delta l = 2$ mm and cyan for 1 mm).

At this point, we would like to mention the details of the volume computation for the melt and crystal, which is performed numerically. In both cases, we sum up the volumes of horizontal trapezoidal slices of height Δh_X and Δh_m , for the crystal and melt, respectively. For $\Delta l = 2$ mm we had $\Delta h_X = 1$ mm and $\Delta h_m = 1 \times 10^{-3}$ mm, and for $\Delta l = 1$ mm we chose $\Delta h_X = 0.5$ mm and $\Delta h_m = 1 \times 10^{-6}$ mm. Δh_m has to be quite small because the melt level is decreasing only very little during necking in the beginning of the growth process. A small value of Δh_m ensures a smooth increase in the growth velocity. At later times, the increase in the growth velocity is quite significant (by up to 45%) and leads to a larger production of latent heat. In particular, we use v_{growth} computed at crystal length l for the latent heat calculation of the computation at $l + \Delta l$. For completeness, we also show the time step Δt , which is computed from the obtained growth velocity and the fixed increase in crystal length. We obtained the upper curve for $\Delta l = 2$ mm (blue curve) and the lower for $\Delta l = 1$ mm (cyan curve). The time step, even for $\Delta l = 1$ mm, is much larger than required for the computation of the dislocation density in MACPLAS.

The solid/liquid interface shapes calculated by the global model are plotted at the bottom of Figure 5. The corresponding deflection is plotted at the top of Figure 5. Initially,

the interface is almost flat. During the shoulder growth, the interface becomes more and more convex. This is at least partly caused by the melt convection, as can be seen from Figure 6 for the velocity field and Figure 7 for the temperature field. The inductive heating causes the hottest region to be in the right lower part of the melt. As a result a convection roll is established, transporting the heat from this right lower part to the three-phase point of crystal, melt, and gas. The rotation of the crystal prevents this convection roll entering the region beneath the crystal, leaving this region with cooler melt. With increasing crystal and decreasing melt level, the buoyancy-induced convection roll becomes weaker and the interface becomes flatter. With the increasing melt level, the counter vortex in the upper outer part of the melt disappears. At $l = 50$ mm in Figure 6 this can be clearly seen, leading to a cold region in the top outer part of the melt (see Figure 7). Note that calculations with neglected melt flow were not performed, so that some effects of the changing global temperature field on the interface deflection cannot be excluded.

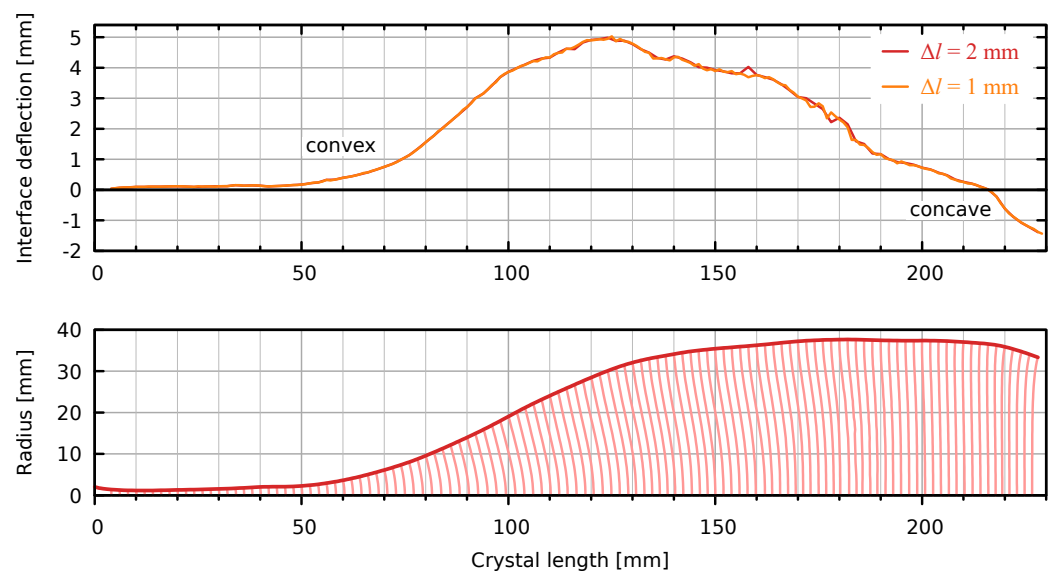


Figure 5. (Top) Deflection of the solid/liquid interface as a function of the growth stage (crystal length). (Bottom) Calculated interface shapes for $\Delta l = 2$ mm plotted for crystal lengths from 4 mm to 228 mm.

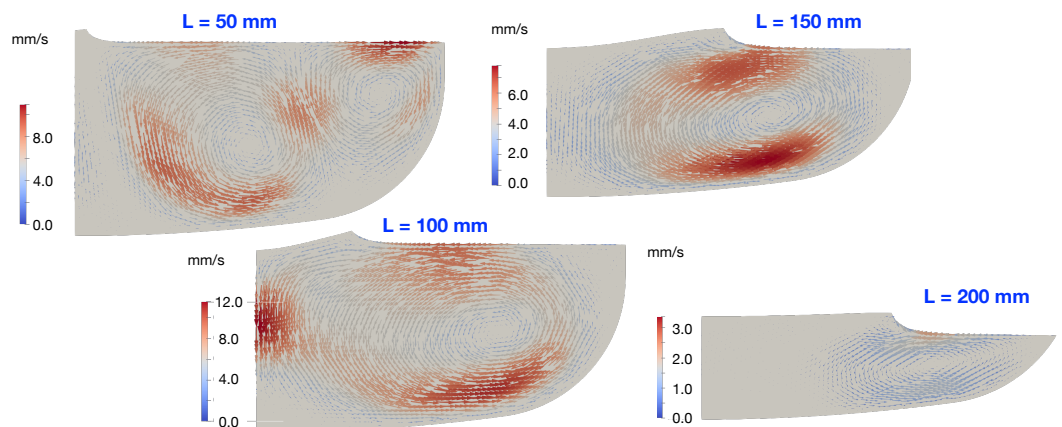


Figure 6. Velocity field in the melt for four growth stages.

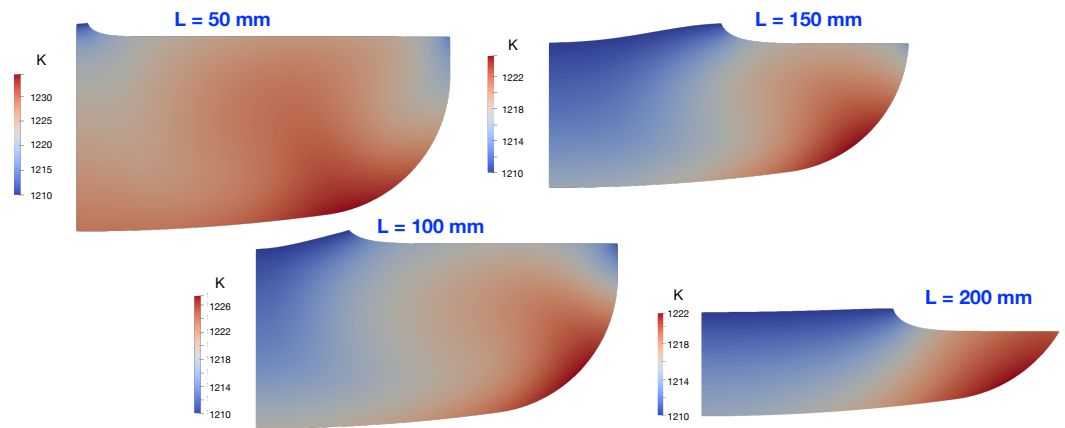


Figure 7. Temperature field in the melt for four growth stages.

Looking in more detail at the deflection in the top part of Figure 5 one sees some oscillations in the deflection curve, less pronounced for $\Delta l = 1$ mm than for $\Delta l = 2$ mm. In both cases, the mesh size in crystal and melt was $1 \text{ mm} \times 1 \text{ mm}$. In addition to questions of spatial resolution, it should be mentioned that we performed quasi-stationary calculations that do not take into consideration the change interface shape from one time step to the next for the computation of the latent heat release at the interface. We had only the latent heat production from the computed overall growth velocity v_{growth} , which is the same all along the interface.

5.2. Local Simulation (MACPLAS)

In MACPLAS we used the crystal shape, including the computed solid/liquid interface shape, as the geometrical input, and use the temperature at the rim of the crystal as the thermal boundary condition. As a check, we compared the stresses (isotropic) for a crystal of length 228 mm. For this purpose a steady-state temperature computation was performed with MACPLAS. The elastic stress calculated by Elmer and MACPLAS was found to be in excellent agreement.

At this point, we have to discuss the stress–strain relation in the axisymmetric case in more detail. For this case Lambropoulos derived modified matrices of elastic constants for two growth directions, $\langle 001 \rangle$ and $\langle 111 \rangle$ [54]. The typical growth direction for HPGe crystals is $\langle 001 \rangle$ and this was also used in our experiment. For this growth direction, the stress–strain relation is

$$\begin{pmatrix} \sigma_{rr} \\ \sigma_{\phi\phi} \\ \sigma_{zz} \\ \sigma_{rz} \end{pmatrix} = \begin{pmatrix} C_{11} + \frac{1}{4}H & C_{12} - \frac{1}{4}H & C_{12} & 0 \\ C_{12} - \frac{1}{4}H & C_{11} + \frac{1}{4}H & C_{12} & 0 \\ C_{12} & C_{12} & C_{11} & 0 \\ 0 & 0 & 0 & C_{44} \end{pmatrix} \begin{pmatrix} \varepsilon_{rr} - \varepsilon_T \\ \varepsilon_{\phi\phi} - \varepsilon_T \\ \varepsilon_{zz} - \varepsilon_T \\ \varepsilon_{rz} \end{pmatrix}, \quad (7)$$

where H is given by $H = 2C_{44} + C_{12} - C_{11}$, i.e., $H = (5.3 \times 10^{10} - 8.6 \times 10^6 \text{ K}^{-1}T)$ Pa for Ge. σ_{ij} and ε_{ij} are the stress and strain components, respectively. The thermal strain is $\varepsilon_T = \bar{\alpha}(T - T_{\text{ref}})$, where T_{ref} is the reference temperature and $\bar{\alpha}$ is the averaged thermal expansion coefficient (calculated from the differential expansion coefficient α_L ; see [34]).

Currently, only the isotropic model with $H = 0$ (i.e., the influence of the growth direction is not considered) is implemented in MACPLAS:

$$\begin{pmatrix} \sigma_{rr} \\ \sigma_{\phi\phi} \\ \sigma_{zz} \\ \sigma_{rz} \end{pmatrix} = \begin{pmatrix} C_{11} & C_{12} & C_{12} & 0 \\ C_{12} & C_{11} & C_{12} & 0 \\ C_{12} & C_{12} & C_{11} & 0 \\ 0 & 0 & 0 & C_{44} \end{pmatrix} \begin{pmatrix} \varepsilon_{rr} - \varepsilon_T - \varepsilon_{rr}^c \\ \varepsilon_{\phi\phi} - \varepsilon_T - \varepsilon_{\phi\phi}^c \\ \varepsilon_{zz} - \varepsilon_T - \varepsilon_{zz}^c \\ \varepsilon_{rz} - \varepsilon_{rz}^c \end{pmatrix}, \quad (8)$$

where the plastic strain components ε_{ij}^c are obtained by integrating Equation (6). Elastic simulations can be carried out by setting $\varepsilon_{ij}^c = 0$. This means that all the results presented later for the dislocation densities are based on the stress computation with $H = 0$. In order to estimate the range of error with this approach, i.e., to evaluate the importance of the anisotropy, we checked the impact of the correction term H on the stress field in a steady-state Elmer computation for a crystal of length 228 mm. The stress distribution is similar in both cases, as can be seen in Figure 8. However, the stress is about 15% larger for the case $H \neq 0$.

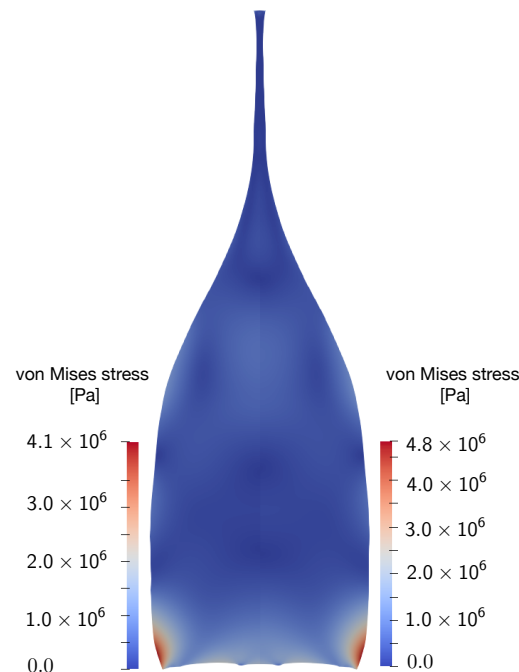


Figure 8. Von Mises stress computed by Elmer. **(Left)** Using symmetric matrix of elastic coefficients. **(Right)** Using approach of Lambropoulos for a crystal grown in the (001) direction [54].

Using the crystal shape and temperature field at the crystal side surface calculated by Elmer, fully transient temperature and dislocation density simulations were carried out using MACPLAS. Since the maximum time step was set to 0.2 s (about three orders of magnitude smaller than the temporal resolution in the Elmer model; see Figure 4), the original Elmer data were interpolated in time, as described in Section 2.2.

The calculated dislocation density in the crystal is shown in Figure 9. The initial density in the entire seed was set to $N_0 = 1 \text{ cm}^{-2}$. At the final time, the maximum dislocation density is three orders of magnitude higher than the initial one. The highest dislocation density is at the crystal side surface; a local N_m maximum develops on the crystal axis, thus, the radial dislocation density distribution has a W-shaped profile (see also [25]). The W-shape can be even better seen in Figure 10, where the radial distribution of the dislocation density is shown for lines at three different vertical positions in the final crystal. These positions correspond to the horizontal cuts for the wafers from the crystal that was grown, and are indicated in Figure 2.

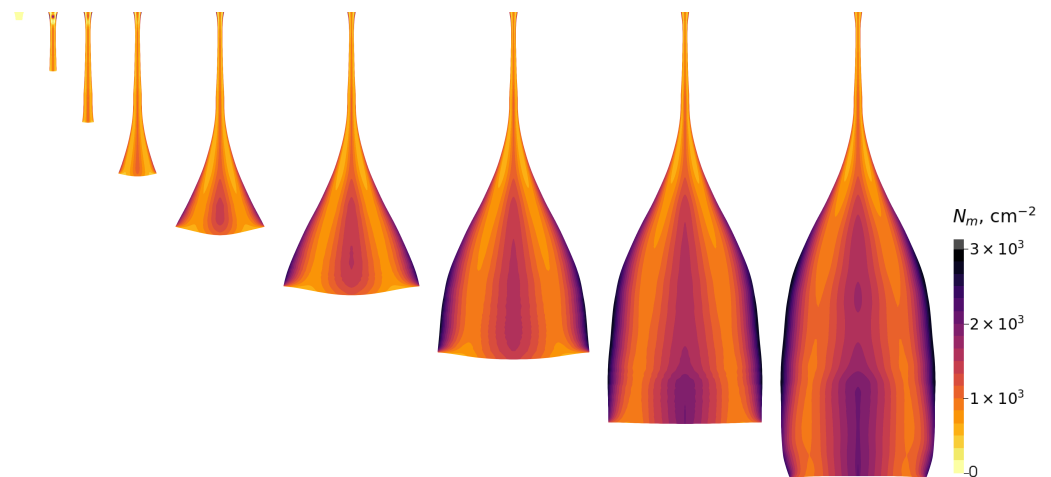


Figure 9. Calculated dislocation density in the crystal at different times. $\Delta l = 1$ mm, the results are shown from left to right, starting at $t = 0$ min each 50 min, including the final distribution at 6:28:46.

The computed dislocation densities are compared to the EPD data on the three wafers. EPD data were taken at the centre and near the edge of the wafer. As can be seen from Figures 10 and 11, a good match is obtained for the first cut ($l = 80$ mm). For the other positions, the dislocation density in the experiment was higher. This discrepancy, even to a greater extent, was already observed in another investigation [25]. We also see in Figure 11 that for the dislocation densities at $l > 180$ mm there is a significant difference between the runs with $\Delta l = 2$ mm (dashed line) and with $\Delta l = 1$ mm (solid line). This indicates that small differences in the interface shapes might lead to a larger difference in dislocation densities at later times. From Figure 5, one can see that the differences are in the sub-millimetre range. Thus, we need a very fine mesh in the region of the interface to reach a high accuracy. Another issue is the computation of the melt convection. Higher accuracy might be achieved by coupling the global simulation of Elmer with the computation of convection by a finite volume code such as OpenFOAM (<https://www.openfoam.com> (accessed on 27 September 2023)), which is better suited for this purpose. A third point on the global simulation is the missing latent heat effect when the interface shape is changing from one time step to the next. This also requires a very fine mesh in the vicinity of the interface, as already mentioned above, and in addition, more inner iteration steps are necessary to converge the coupled system of geometrical change, latent heat production, and melt convection.

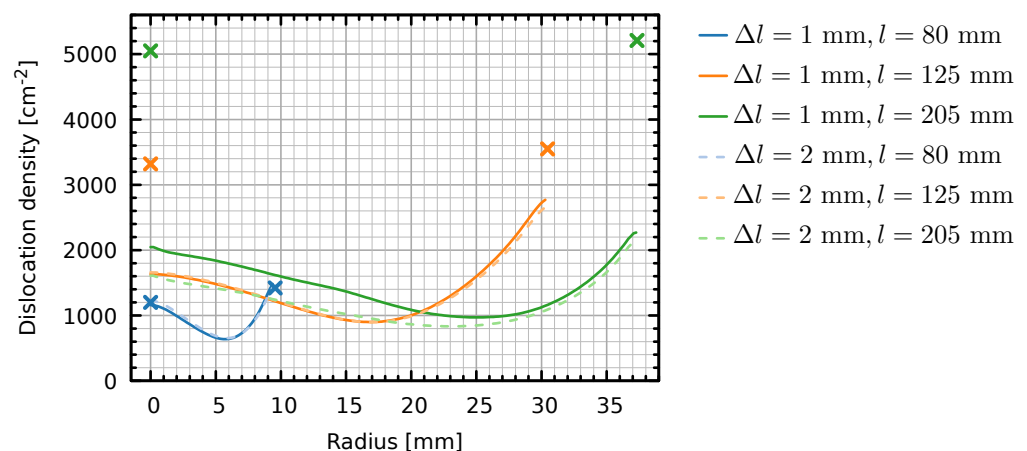


Figure 10. Radial dislocation density distributions at different crystal lengths for $\Delta l = 1$ mm (solid lines) and $\Delta l = 2$ mm (dashed lines). \times : Experimental values for the corresponding wafers.

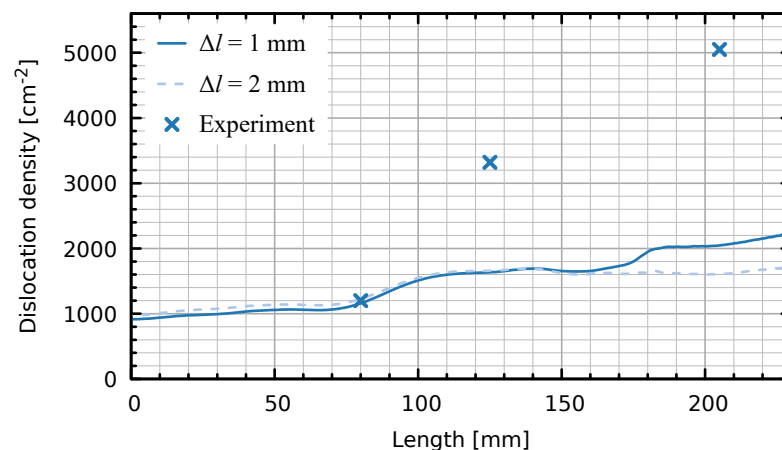


Figure 11. Comparison of axial dislocation density distributions.

There might also be several reasons at the level of the local calculations for the discrepancy between the computed dislocation density and EPD:

- We use a quasi-transient approach for the global thermal calculation.
- For the stress calculation, $H = 0$ was used in Equation (7) and not Lambropoulos' approximation for growth in the $\langle 100 \rangle$ direction.
- We used a simple AH model without considering glide planes [55].
- The AH model is a local model in the sense that dislocations do not propagate from one computational node to a neighbouring one.

The last point in the list is important from an experimental point of view. In the end of the growth process, the crystal is detached from the melt or the melt is consumed completely. In both cases, there is a strong tendency of dislocation multiplication at the end of the crystal running back into the bulk volume. Such a propagation of dislocation from the end of the crystal towards the central bulk region is not covered by the Alexander–Haasen model. This could significantly influence the final dislocation density at $l = 205$ mm. In order to study this in detail, a mapping of the etch pit densities over larger areas is required. This would allow a broader comparison between the experimental and numerical results. A better understanding of the dislocation dynamics in the middle of the growth process, both by further developing the numerical approach as well as a more detailed dislocation density distribution study along the crystal, will be the prerequisite for defining possible strategies for dislocation engineering.

6. Conclusions

We have developed a uni-directional coupling of global axisymmetric calculations using the open source package Elmer with local axisymmetric calculations of dislocation densities in the crystal using the software tool MACPLAS. The local simulations apply a series of crystal shapes (including melt/crystal interface) as the geometrical input and the series of temperature distributions at the rim of the crystal as thermal boundary conditions for the calculations. The local simulation is a transient calculation with a much smaller time step than the series of global computations. Therefore, geometrical and thermal boundary conditions are interpolated.

This numerical approach has been applied to the Czochralski growth of high-purity germanium, where inductive heating is used. We performed one experiment for comparison with the computations. The shape of the crystal grown in the experiment was used in the computations. In the global simulation of the temperature field, the heater power was changed by an algorithm to keep the temperature at the three-phase point at melting point temperature. This change in power was in good agreement with the change in the power in the experiment.

The etch pit density (EPD) was measured for three wafers from different parts of the crystal. The computed dislocation density at the top part (shoulder) agrees well with the EPD. In the further growth phases, the dislocation density in the simulation does not increase so much as in the experiment and, thus, we have the largest disagreement for the wafer at the end of the cylindrical part. There might be several reasons for this discrepancy. On the level of global simulations the calculation of the melt convection, i.e., crystallisation interface shape should be improved. In the computation of dislocation densities there are several options to extend the simple Alexander–Haasen model. A more systematic study, with more experiments exploiting the EPD at several locations, will be important and will be carried out as a next step.

Author Contributions: Conceptualisation, W.M., A.S., R.S. and A.G.; Formal analysis, W.M. and A.S.; funding acquisition, A.S. and R.S.; investigation, W.M., A.S., A.G. and K.-P.G.; methodology, W.M., A.S., A.W. and K.D.; project administration, A.S. and R.S.; software, W.M., A.S. and A.W.; supervision, J.V., K.D. and R.S.; validation, W.M., A.S. and K.D.; visualisation, W.M. and A.S.; writing—original draft, W.M., A.S., K.-P.G. and A.W.; writing—review and editing, R.S., J.V. and K.D. All authors have read and agreed to the published version of the manuscript.

Funding: A.S. acknowledges financial support from the PostDoc Latvia Project No. 1.1.1.2/VIAA/2/18/280. K.-P.G. and R.S. thank BMBF for the research grant, LEGEND (No. 05A20BC2). K.D. and A.W. have received funding from the European Research Council (ERC) under the European Union’s Horizon 2020 research and innovation programme (grant agreement no. 851768).

Data Availability Statement: Data are available on request.

Conflicts of Interest: The authors declare no conflict of interest.

Appendix A

The thermal conductivity of solid Ge has been measured as a function of temperature by Glasbrenner and Slack [56]. The temperature dependent behaviour can be divided into three regions (see Figure A1). Above 1000 K the thermal conductivity is constant, with a value of $\lambda = 17 \text{ W m}^{-1} \text{ K}^{-1}$.

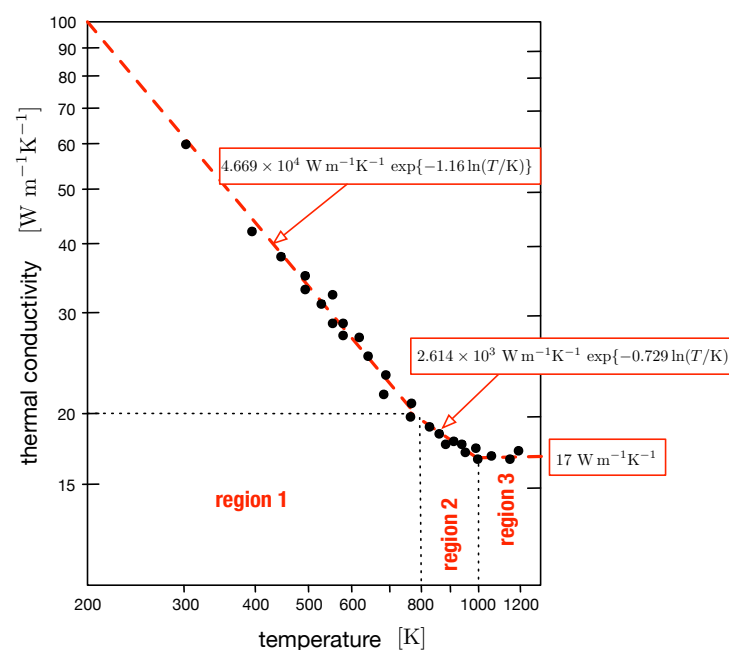


Figure A1. Heat conductivity measured by Glasbrenner and Slack (see Figure 3 in [56]). The heat conductivity is approximated by three different functions for regions 1 ($T < 800 \text{ K}$), 2 ($800 \text{ K} \leq T \leq 1000 \text{ K}$), and 3 ($T > 1000 \text{ K}$), respectively.

Reeber and Wang measured the thermal expansion of Ge crystals [47], which is shown in Figure A2. In our computations, only the temperature regime with $T > 300$ K is of interest, where the data points can be presented by the function given in the figure.

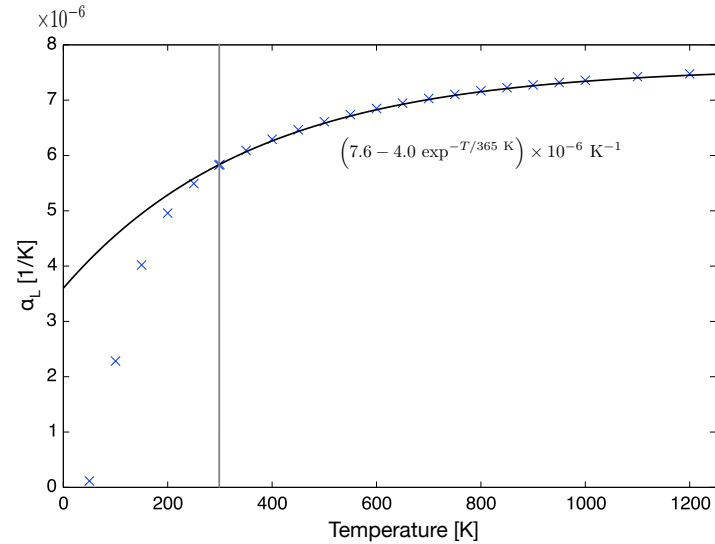


Figure A2. Thermal expansion coefficient measured by Reeber and Wang [47]. We approximate the data by the function represented by the black line. It is a good approximation for the relevant temperature range 300–1200 K.

The measured data for the elastic coefficients by Nikanarov [57] are shown in Figure A3. In the relevant temperature regime for our calculations ($T > 500$ K), all coefficients can be approximated by a linear dependence on the temperature. Please note that in our previous paper [9] there was an error when applying the scale for C_{44} , which leads to different functions both for C_{44} and C_{12} .

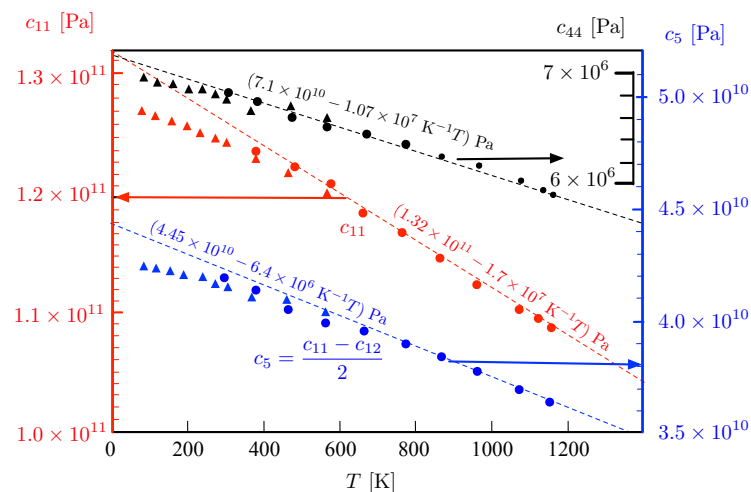


Figure A3. Elastic constants for Ge. Figure of measured data is taken from [58], which is based on [57]. We approximated the data with linear functions, represented by dashed lines.

References

1. Moskalyk, R. Review of germanium processing worldwide. *Miner. Eng.* **2004**, *17*, 393–402. [[CrossRef](#)]
2. Curtolo, D.C.; Friedrich, S.; Friedrich, B. High Purity Germanium, a Review on Principle Theories and Technical Production Methodologies. *J. Cryst. Process Technol.* **2017**, *7*, 65–84. [[CrossRef](#)]
3. Haller, E.E.; Hansen, W.L.; Goulding, F.S. Physics of ultra-pure germanium. *Adv. Phys.* **1981**, *30*, 93–138. [[CrossRef](#)]
4. Moskovskih, V.A.; Kasimkin, P.V.; Shlegel, V.N.; Vasiliev, Y.V.; Gridchin, V.A.; Podkopaev, O.I. The low thermal gradient CZ technique as a way of growing of dislocation-free germanium crystals. *J. Cryst. Growth* **2014**, *401*, 767–771. [[CrossRef](#)]

5. Cattadori, C.M.; Salamida, F. GERDA and LEGEND: Probing the Neutrino Nature and Mass at 100 meV and beyond. *Universe* **2021**, *7*, 314. [CrossRef]
6. Agostini, M.; Allardt, M.; Bakalyarov, A.M.; Balata, M.; Barabanov, I.; Baudis, L.; Bauer, C.; Bellotti, E.; Belogurov, S.; Belyaev, S.T.; et al. Background-free search for neutrinoless double- β decay of ^{76}Ge with GERDA. *Nature* **2017**, *544*, 47. [CrossRef]
7. Van den Bogaert, N.; Dupret, F. Dynamic global simulation of the Czochralski process II. Analysis of the growth of a germanium crystal. *J. Cryst. Growth* **1997**, *171*, 77–93. [CrossRef]
8. Artemyev, V.V.; Smirnov, A.D.; Kalaev, V.V.; Mamedov, V.M.; Sidko, A.P.; Podkopaev, O.I.; Kravtsova, E.D.; Shimansky, A.F. Modeling of dislocation dynamics in germanium Czochralski growth. *J. Cryst. Growth* **2017**, *468*, 443–447. [CrossRef]
9. Miller, W.; Abrosimov, N.; Fischer, J.; Gybin, A.; Juda, U.; Kayser, S.; Janicskó-Csáthy, J. Quasi-Transient Calculation of Czochralski Growth of Ge Crystals Using the Software Elmer. *Crystals* **2020**, *10*, 18. [CrossRef]
10. Alexander, H.; Haasen, P. Dislocations and plastic flow in the diamond structure. In *Solid State Physics*; Seitz, F., Turnbull, D., Ehrenreich, H., Eds.; Elsevier: Amsterdam, The Netherlands, 1969; Volume 22, pp. 27–158. [CrossRef]
11. Gradwohl, K.P.; Roder, M.; Danilewsky, A.N.; Sumathi, R.R. Investigation of the dislocation structure in Czochralski germanium crystals grown in [211] and [110] growth direction. *CrystEngComm* **2021**, *23*, 4116–4124. [CrossRef]
12. Gradwohl, K.P.; Miller, W.; Dropka, N.; Sumathi, R.R. Quantitative dislocation multiplication law for Ge single crystals based on discrete dislocation dynamics simulations. *Comput. Mater. Sci.* **2022**, *211*, 111537. [CrossRef]
13. Bános, N.; Friedrich, J.; Müller, G. Simulation of dislocation density: Global modeling of bulk crystal growth by a quasi-steady approach of the Alexander–Haasen concept. *J. Cryst. Growth* **2008**, *310*, 501–507. [CrossRef]
14. Gao, B.; Nakano, S.; Kakimoto, K. Highly efficient and stable implementation of the Alexander–Haasen model for numerical analysis of dislocation in crystal growth. *J. Cryst. Growth* **2013**, *369*, 32–37. [CrossRef]
15. Lu, S.; Chen, H.; Hang, W.; Wang, R.; Yuan, J.; Pi, X.; Yang, D.; Han, X. Numerical analysis of the dislocation density in the n-type 4H-SiC. *CrystEngComm* **2023**, *25*, 3718–3725. [CrossRef]
16. Miyazaki, N.; Okuyama, S. Development of finite element computer program for dislocation density analysis of bulk semiconductor single crystals during Czochralski growth. *J. Cryst. Growth* **1998**, *183*, 81–88. [CrossRef]
17. Miyazaki, N.; Kuroda, Y.; Sakaguchi, M. Dislocation density analyses of GaAs bulk single crystal during growth process (effects of crystal anisotropy). *J. Cryst. Growth* **2000**, *218*, 221–231. [CrossRef]
18. Gallien, B.; Albaric, M.; Duffar, T.; Kakimoto, K.; M’Hamdi, M. Study on the usage of a commercial software (Comsol-Multiphysics®) for dislocation multiplication model. *J. Cryst. Growth* **2017**, *457*, 60–64. [CrossRef]
19. Pendurti, S. Modeling Dislocation Generation in High Pressure Czochralski Growth of InP Single Crystals. Ph.D. Thesis, State University of New York, Stony Brook, NY, USA, 2003.
20. Mamedov, V.; STR Group—Soft-Impact, Ltd., St. Petersburg, Russia. Private communication.
21. Wang, G.; Guan, Y.; Mei, H.; Mei, D.; Yang, G.; Govani, J.; Khizar, M. Dislocation density control in high-purity germanium crystal growth. *J. Cryst. Growth* **2014**, *393*, 54–58. [CrossRef]
22. Abrosimov, N.; Czupalla, M.; Dropka, N.; Fischer, J.; Gybin, O.; Irmscher, K.; Janicskó-Csáthy, J.; Juda, U.; Kayser, S.; Miller, W.; et al. Technology Development of High Purity Germanium Crystals for Radiation Detectors. *J. Cryst. Growth* **2020**, *532*, 125396. [CrossRef]
23. Sumathi, R.R.; Gybin, A.; Gradwohl, K.P.; Palleti, P.C.; Pietsch, M.; Irmscher, K.; Dropka, N.; Juda, U. Development of Large-Diameter and Very High Purity Ge Crystal Growth Technology for Devices. *Cryst. Res. Technol.* **2023**, *58*, 2200286. [CrossRef]
24. MACPLAS: MACroscopic Crystal PLAsticity Simulator. Available online: <https://github.com/aSabanskis/MACPLAS> (accessed on 1 September 2023).
25. Sabanskis, A.; Dadzis, K.; Gradwohl, K.P.; Wintzer, A.; Miller, W.; Juda, U.; Sumathi, R.R.; Virbulis, J. Parametric numerical study of dislocation density distribution in Czochralski-grown germanium crystals. *J. Cryst. Growth* **2023**, *622*, 127384. [CrossRef]
26. Available online: <https://www.csc.fi/web/elmer> (accessed on 1 September 2023).
27. Geuzaine, C.; Remacle, J.F. Gmsh: A 3-D finite element mesh generator with built-in pre- and post-processing facilities. *Int. J. Numer. Methods Eng.* **2009**, *79*, 1309–1331. [CrossRef]
28. Available online: <https://github.com/nemocrys/objectgmsh> (accessed on 1 September 2023). [CrossRef]
29. Available online: <https://github.com/nemocrys/pyelmer> (accessed on 1 September 2023).
30. Available online: <https://github.com/nemocrys/opencgs> (accessed on 1 September 2023).
31. Enders-Seidlitz, A.; Pal, J.; Dadzis, K. Development and validation of a thermal simulation for the Czochralski crystal growth process using model experiments. *J. Cryst. Growth* **2022**, *593*, 126750. [CrossRef]
32. Hurlle, D.T.J. Analytical representation of the shape of the meniscus in Czochralski growth. *J. Cryst. Growth* **1983**, *63*, 13–17. [CrossRef]
33. Arndt, D.; Bangerth, W.; Davydov, D.; Heister, T.; Heltai, L.; Kronbichler, M.; Maier, M.; Pelteret, J.P.; Turcksin, B.; Wells, D. The deal.II library, version 8.5. *J. Numer. Math.* **2017**, *25*, 137–145. [CrossRef]
34. Sabanskis, A.; Dadzis, K.; Menzel, R.; Virbulis, J. Application of the Alexander–Haasen Model for Thermally Stimulated Dislocation Generation in FZ Silicon Crystals. *Crystals* **2022**, *12*, 174. [CrossRef]
35. Rhim, W.K.; Ishikawa, T. Thermophysical Properties of Molten Germanium Measured by a High-Temperature Electrostatic Levitator. *Int. J. Thermophys.* **2000**, *21*, 429–443. [CrossRef]

36. Chathoth, S.M.; Damaschke, B.; Samwer, K.; Schneider, S. Thermophysical properties of Si, Ge, and Si–Ge alloy melts measured under microgravity. *Appl. Phys. Lett.* **2008**, *93*, 071902. [\[CrossRef\]](#)
37. Nishi, T.; Shibata, H.; Ohta, H. Thermal Diffusivities and Conductivities of Molten Germanium and Silicon. *Mater. Trans.* **2003**, *44*, 2369–2374. [\[CrossRef\]](#)
38. Takasuka, E.; Tokizaki, E.; Terashima, K.; Kimura, S. Emissivity of liquid germanium in visible and near infrared region. *J. Appl. Phys.* **1997**, *82*, 2590–2594. [\[CrossRef\]](#)
39. Skinner, L.; Barnes, A.C. An oscillating coil system for contactless electrical conductivity measurements of aerodynamically levitated melts. *Rev. Sci. Instrum.* **2006**, *77*, 123904. [\[CrossRef\]](#)
40. Sato, Y.; Nishizuka, T.; Tachikawa, T.; Hoshi, M.; Yamamura, T.; Yamamura, T. Viscosity and density of molten germanium. *High Temp. High Press.* **2000**, *32*, 252–260. [\[CrossRef\]](#)
41. Artemyev, V.K.; Folomeev, V.I.; Ginkin, V.P.; Kartavykh, A.V.; Mil'vidskii, M.G.; Rakov, V.V. The mechanism of Marangoni convection influence on dopant distribution in Ge space-grown single crystals. *J. Cryst. Growth* **2001**, *223*, 29–37. [\[CrossRef\]](#)
42. den Bogaert, N.V.; Dupret, F. Dynamic global simulation of the Czochralski process I. Principles of the method. *J. Cryst. Growth* **1997**, *171*, 65–76. [\[CrossRef\]](#)
43. Allen, F.G. Emissivity at 0.65 Micron of Silicon and Germanium at High Temperatures. *J. Appl. Phys.* **1957**, *28*, 1510–1511. [\[CrossRef\]](#)
44. Hellwege, K.H.; Madelung, O. (Eds.) *Landolt-Börnstein*; Springer: Berlin, Germany, 1984; Volume 22a.
45. Haasen, P. Dislocations in Semiconductors. *J. Phys. Colloques* **1966**, *27*, C3-30–C3-38. [\[CrossRef\]](#)
46. Schaumburg, H. Velocity Measurements on Screw- and 60°-Dislocations in Germanium. *Phys. Status Solidi (B)* **1970**, *40*, K1–K4. [\[CrossRef\]](#)
47. Reeber, R.R.; Wang, K. Thermal expansion and lattice parameters of group IV semiconductors. *Mater. Chem. Phys.* **1996**, *46*, 259–264. [\[CrossRef\]](#)
48. Schunk. *Data Sheet Schunk Carbon Group*; Schunk Kohlenstofftechnik GmbH: Heuchelheim, Germany, private communication.
49. Moroe, S.; Woodfield, P.L.; Kimura, K.; Kohno, M.; Fukai, J.; Fuji, M.; Shinzato, K.; Takata, Y. Measurements of Hydrogen Thermal Conductivity at High Pressure and High Temperature. *Int. J. Thermophys.* **2011**, *32*, 1887–1917. [\[CrossRef\]](#)
50. Sakoda, N.; Hisatsugu, T.; Furusato, K.; Shinzato, K.; Kohno, M.; Takata, Y. Viscosity measurements of hydrogen at high temperatures up to 573 K by a curved vibrating wire method. *J. Chem. Thermodyn.* **2015**, *89*, 22–26. [\[CrossRef\]](#)
51. Wagner, S. IEEE standard test procedures for high-purity germanium crystals for radiation detectors. *IEEE Std 1160* **1993**, *1993*, 20–21.
52. Abrosimov, N.V.; Lüdge, A.; Riemann, H.; Schröder, W. Lateral photovoltage scanning (LPS) method for the visualization of the solid-liquid interface of Si_{1-x}Ge_x single crystals. *J. Cryst. Growth* **2002**, *237–239*, 356–360. [\[CrossRef\]](#)
53. Foroushani, S.; Wintzer, A.; Dadzis, K. Heating efficiency and energy saving potential of a model crystal growth furnace. In Proceedings of the Deutsche Kristallzüchtungstagung (DKT 2023), Augsburg, Germany, 15–17 March 2023. [\[CrossRef\]](#)
54. Lambropoulos, J.C. The isotropic assumption during the Czochralski growth of single semiconductors crystals. *J. Cryst. Growth* **1987**, *84*, 349–358. [\[CrossRef\]](#)
55. Sumino, K.; Yonenaga, I. Dislocation Dynamics and Mechanical Behaviour of Elemental and Compound Semiconductors. *Phys. Status Solid (A)* **1993**, *138*, 573–581. [\[CrossRef\]](#)
56. Glassbrenner, C.J.; Slack, G.A. Thermal Conductivity of Silicon and Germanium from 3 K to the Melting Point. *Phys. Rev.* **1964**, *134*, A1058–A1069. [\[CrossRef\]](#)
57. Nikanorov, S.P.; Kardashev, B.K. *Elasticity and Dislocation Inelasticity of Crystals*; Nauka Publishing House: Moscow, Russia, 1985.
58. Ge—Germanium. Mechanical Properties, Elastic Constants, Lattice Vibrations. Available online: <http://www.ioffe.ru/SVA/NSM/Semicond/Ge/mechanic.html> (accessed on 1 September 2023).

Disclaimer/Publisher's Note: The statements, opinions and data contained in all publications are solely those of the individual author(s) and contributor(s) and not of MDPI and/or the editor(s). MDPI and/or the editor(s) disclaim responsibility for any injury to people or property resulting from any ideas, methods, instructions or products referred to in the content.